Title: Measuring Compound Eye Optics with Microscope and MicroCT Images

Article Type: Methods

Author Names and Affiliations: John Paul Currea[1], Yash Sondhi[2], Akito Y. Kawahara[3], and Jamie Theobald[2]

[1]Department of Psychology, Florida International University, Miami, FL 33199, U.S.A.

[2]Department of Biological Sciences, Florida International University, Miami, FL 33199, U.S.A.

[3]Florida Museum of Natural History, University of Florida, Gainesville, FL, 32611, U.S.A.

Abstract (<200 words):

The arthropod compound eye is the most prevalent eye type in the animal kingdom, with an impressive range of shapes and sizes. Studying its natural range of morphologies provides insight into visual ecology, development, and evolution. In contrast to the camera-type eyes we possess, external structures of compound eyes often reveal resolution, sensitivity, and field of view if the eye is spherical. Non-spherical eyes, however, require measuring internal structures using imaging technology like MicroCT (µCT). µCT is a burgeoning 3D X-Ray imaging technique that has been used to image arthropod muscles, brains, ocelli, and eyes. Thus far, there is no efficient tool to automate characterizing compound eye optics in either 2D or 3D data. We present two open-source programs: (1) the ommatidia detecting algorithm (ODA), which automatically measures ommatidia count and diameter in 2D images, and (2) a µCT pipeline (ODA-3D), which calculates anatomical acuity, sensitivity, and field of view across the eye by applying the ODA to 3D data. We validate these algorithms on images, images of replicas, and µCT scans from eyes of ants, fruit flies, moths, and a bee.

There are about 1.3 million described arthropod species, representing about 80% of described animal species (Zhang 2013). They range vastly in size, lifestyle, and habitat, with body lengths from the 85 µm ectoparasitic crustacean *Tantulacus dieteri* (Mohrbeck, Arbizu, and Glatzel 2010) to the 0.5 m green rock lobster, *Sagmariasus verreauxi* (Holthuis 1991; Kensler 1967), and occupying nearly every ecological niche. Likewise, arthropods wield an array of eye architectures, most commonly the compound eye (Cronin et al. 2014; Land and Nilsson 2012). Recent progress understanding compound eye development facilitates studying the selective pressures on the development of compound eyes (Casares and McGregor 2020; Currea, Smith, and Theobald 2018; Friedrich 2003; Gaspar et al. 2019; Harzsch and Hafner 2006). Arthropod compound eyes are therefore a prime subject in the study of vision (Cronin et al. 2014; Land and Nilsson 2012): they are the most prevalent type in the animal kingdom, and include a variety of morphologies that emerge from relatively well-understood development.

Eye morphology is fundamental to how animals see because structure physically limits visual capacity (Land and Nilsson 2012). Depending on light level and image motion, some optimal eye architecture will maximize the ability to differentiate brightness levels and resolve spatial details (Land 1997; Snyder, Laughlin, and Stavenga 1977; Snyder, Stavenga, and Laughlin 1977). The critical role of morphology implies that natural compound eye diversity will provide insight into visual ecology, development, and evolution. Here we offer two open-source programs written in Python to characterize compound eyes: (1) the ommatidia detecting algorithm (ODA), which automatically detects the individual facets, (called ommatidia), in 2D images, and (2) a multi-stage µCT pipeline (ODA-3D) which applies the ODA to segment individual crystalline cones and characterize the visual field.

In contrast to the camera-type eyes we possess, many structures that limit optical quality in compound eyes are externally visible. A compound eye is composed of many individual ommatidia, each of which has a lens and crystalline cone that direct light onto photoreceptors. Ommatidia usually represent the maximal individual pixels of the transduced image, so their number limits the total number of images an eye can form, or its spatial information capacity, and they can be counted in microscope images. Their count ranges from ~20 ommatidia in the eye of one of the smallest flying insects, the fairyfly *Kikiki huna* (body length=158µm; Huber and Beardsley 2000; Huber and Noyes 2013) to >30,000 in large dragonflies, which have enhanced vision for hunting prey (Cronin et al. 2014).

In each ommatidium, the -lens size restricts aperture, which limits the rate of light collection. This becomes crucially important when photons are limited, such as in dim light, or during fast image

motion (Snyder, Laughlin, et al. 1977; Snyder, Stavenga, et al. 1977; Theobald 2017; Warrant 1999). Compound eyes divide into two structural groups which collect light differently. Apposition eyes separate light with pigment cells between ommatidia, and restrict it to a single rhabdom such that lens size directly limits optical sensitivity (Figure 1A). Superposition eyes direct light through a clear zone, so many facets can contribute to each point in an image (Figure 1B), thereby multiplying final sensitivity (although the image remains subject to the diffraction limit of individual aperture size).

Ommatidia count and diameter can be derived from 2D images. Although several algorithms and software plugins have been proposed to extract ommatidia, they require user input for each image, and underestimate ommatidia counts (Woodman, Todd, and Staveley 2011), overestimate ommatidial diameter (Schramm et al. 2015), or were not validated against manual measurements or measurements in the literature (Diez-Hermano et al. 2015; Iyer et al. 2016; Vanhoutte, Michielsen, and Stavenga 2003). In addition, none are tested on multiple species, over a substantial range of eye sizes, or with different media. To support this effort, we offer an open-source program written in Python called the ODA. We test the reliability and validity of this technique on single images of 6 eye molds of 5 different ant species ranging dramatically in size, microscope images of 39 fruit flies (*Drosophila melanogaster*), and processed images of MicroCT (µCT) scans of 2 moths (*Manduca sexta* and *Deilephila elpenor*) and one bee (*Bombus terrestris*). The method is widely accessible because it only requires microscope imaging.

For spherical eyes, the lens diameter measurements provided by the ODA can be combined with measurements of eye radius (using the luminous pseudopupil technique, for instance) to measure the angular separation of ommatidia, called the interommatidial (IO) angle (Figure 1 $\Delta\varphi$). This angle inversely limits spatial acuity or resolution (Land 1997; Snyder, Laughlin, et al. 1977; Snyder, Stavenga, et al. 1977). High spatial acuity affords many behaviors, such as prey, predator, and mate detection, and perceiving small changes in self-motion (Land 1997; Land and Nilsson 2012). For spherical eyes, the IO angle is approximately: $\Delta\varphi = D/R$, where D is the ommatidial lens diameter and R is the radius of curvature, assuming the axes of all ommatidia converge to a central point. Fortunately, many compound eyes are safely approximated by the spherical model. Smaller compound eyes are often spherical and homogenous because photon noise and diffraction constrain IO angle and ommatidial size (Snyder, Stavenga, et al. 1977). Likewise, superposition eyes are often roughly spherical because they optically combine light from many ommatidia (Figure 1B; Land and Nilsson 2012).

But many compound eyes are non-spherical, with ommatidial axes askew to the eye surface. Skewed ommatidia sacrifice sensitivity by reducing the effective aperture as a function of the skewness angle and refraction, but can improve acuity at the expense of field of view (FOV) by pointing more ommatidia onto a small visual field (Figure 1C). Alternatively, skewness can increase FOV at the expense of acuity by spreading a few ommatidia over a large visual field (Figure 1D).

MicroCT (µCT), a 3D X-Ray imaging technique burgeoning in use among comparative morphologists (Baird and Taylor 2017; Buser et al. 2020), is a rich and valuable resource to study arthropod vision. It has been used on arthropods to study muscles (Walker et al. 2014), brains (Smith et al. 2016), ocelli (Taylor et al. 2016), and eyes (Brodrick et al. 2020; Gaspar et al. 2019; Taylor et al. 2018, 2020). Visualizing internal structures in 3D allows calculating visual parameters for non-spherical compound eyes, measuring anatomical IO angles at very high spatial resolution, and segmenting different tissues, such as visual neuropils, within the same dataset.

Our second proposed method, ODA-3D, extracts crystalline cones from a µCT image stack (using the ODA) to measure the size, orientation, and spatial distribution of ommatidia. As mentioned above, we validate it on µCT scans of the spherical eyes of two moth species (*M. sexta* and *D. elpenor*) collected by us and an open access scan of a non-spherical, oval bumblebee eye (*B. terrestris*) used in Taylor et al. (2018). For the bumblebee, we further demonstrate how ODA-3D can detect oval eye features, measure regional changes in skewness, spatial acuity, and sensitivity, and project onto world-referenced coordinates to more accurately measure FOV.

Compound eyes are the most common image-forming structures on earth. Because there are so many arthropod species and compound eye morphologies, it is challenging but valuable to characterize them in a meaningful, fast manner. Our proposed methods minimize the substantial labor that is typically required in characterizing optical performance in compound eyes and therefore facilitate understanding their role in visual ecology, development, and evolution.

Methods

Specimens

Microscope images of eye molds or replicas were taken previously on five ant species: *Notoncus ectatommoides* and a Golden tail sugar ant (*Camponotus aeneopilosus*) of the Formicinae subfamily (from Palavalli-Nettimi and Narendra (2018)), a jumper ant (*Myrmecia nigrocincta*) and a bull ant (*M.*

tarsata) of the Myrmeciinae subfamily, and *Rhytidoponera inornata* of the Ectatomminae subfamily (from Palavalli-Nettimi et al. (2019)). We further used microscope images of 39 fruit fly eyes (*Drosophila melanogaster*) from Currea et al. (2018).

We obtained micro-computed tomographs (µCTs) of the tobacco hornworm (*Manduca sexta*), the elephant hawkmoth (*Deilephila elpenor*), and the bumblebee (*Bombus terrestris*). Vouchered moth specimens from the Florida Natural History Museum were stored at -20°C in 95% ethanol, then heads were sliced, with antennae removed, and soaked in staining solution (I2+KI, equal proportions 1.25% I2 and 2.5% KI solutions) in Eppendorf vials or falcon tubes for 36–48 hours. *M. sexta* was scanned with a Phoenix V|Tome|X M system with: a 180kv x-ray tube, a diamond-tungsten target, 80 kV tube voltage, 110 µA current, 17.8 mm source object distance, 793 mm object-detector distance, and capture time adjusted to maximize absorption range for each scan. The acquisition consisted of 2300 projections, 8 s each. GE's datos|x r software version 2.3 processed raw x-ray data, producing voxel size of 4.50074 µm. Volume files were imported into VG StudioMax version 3.3.3 (Volume Graphics, Heidelberg, Germany), eyes isolated with the segmentation tools, then exported as Tiff stacks. *D. elpenor* was scanned with a Zeiss Xradia 520 Versa (Carl Zeiss Microscopy GmbH, Jena, Germany), with: 80 kV tube voltage, 88 µA current, low energy filtering, 22.5 mm source object distance, 210 mm object-detector distance, an indirect detector comprising a scintillator, a 0.392x optical lens, and a camera. The acquisition consisted of 3201 projections, 8 s each, with the adaptive motion correction option in Scout-and-Scan software (Carl Zeiss Microscopy GmbH). The tomographic reconstruction automatically generated a 32-bit txrm set of tomograms with an isotropic voxel size of 3.3250 µm. The XRM controller software (Carl Zeiss Microscopy GmbH) converted data to a stack of 16-bit tiff file. A previously scanned bumblebee eye was used with permission from the authors, available at https://www.morphosource.org/Detail/ProjectDetail/Show/project_id/646. This sample was scanned with a synchrotron x-ray source, (Baird and Taylor 2017), see Taylor et al., (2018) for the details.

Ommatidia Detecting Algorithm

Fourier transforms decompose arbitrary functions into component sinusoids, which can highlight periodic patterns. For digital images, the sinusoidal elements of a 2D Fast Fourier Transform (FFT) are plane waves (gratings), characterized by contrast, frequency, phase, and orientation. Operations applied to the frequency representation (reciprocal space) can be inverse-transformed to generate a filtered image. The hexagonal arrangement of typical ommatidia has 3 major axes (Figure 2 B), each

approximated by a grating, and filtering frequencies higher than these generates a smooth image, with peaks near ommatidia centers that are easily detected with local maxima detection algorithms.

We developed a Python language module, the ommatidia detecting algorithm (ODA), which: (1) generates a 2D FFT, (2) finds the three fundamental gratings as the local maxima closest to the reciprocal image center, (3) filters higher image frequencies, (4) inverts the filtered 2D FFT, and (5) finds local maxima in the smoothed image (Figure 2 B). Users optionally check results in the reciprocal image with maxima superimposed. The program stores ommatidia coordinates and calculates ommatidial diameter. An optional imported mask (a white silhouette on a black background) can help avoid false positives outside of the eye. This program is available for download at www.github.com/jpcurrea/fly_eye/, including basic examples on how to use it.

Measuring Ommatidia using µCT

We have further used the ODA to process 3D µCT data. This pipeline: (1) imports a stack of images representing a 3D dataset of points in the crystalline cones (Figure 3 A). Images can be edited to delete irrelevant pixels, and our program can pre-filter data by choosing a density range in a graphical interface, to further isolate crystalline cones, and can preview the whole dataset (Figure 4 A).

(2) projects coordinates onto 2D images and processes with the ODA (Figure 3 B). The layer of crystalline cones curves with little variation normal to its surface, allowing a sphere fit with least squares regression. The algorithm transforms points to spherical coordinates and interpolates a continuous surface, modeling the points' radii as a function of elevation and azimuth. Finally, it partitions coordinates into shells of points inside and outside of the fitted surface (Figure 4 B).

(3) forms images of each shell by taking 2D histograms of elevation and azimuth (ignoring radius, Figure 3 C). Processing coordinates in 90°X90° segments, recentered before forming the histogram, avoids extreme spherical warping. The ODA approximates lens centers within each segment, then recombines them into the original coordinate system by finding the nearest groups of points between each shell. Finally, each point is labeled by its nearest center, effectively segmenting points into clusters of separate crystalline cones (Figure 4 C). Although Steps 2 and 3 work well for spherical eyes, when ommatidia are substantially skewed the offset between inside and outside shells prevents the algorithm from segmenting points into correct clusters, excluding them from the count. Therefore our program has an option for non-spherical ommatidia distributions where, instead of two shells in step 2, we extract one shell around the fitted surface containing 50% of residuals (Figure 4 B). Then as in 3,

we partition the eye into 90° x 90° segments and find cluster centers with the ODA (Figure 4 C *top* and *middle*). We use the number of ommatidia from the algorithm to apply the spectral clustering algorithm to the total collection of points (Figure 4 C *bottom*), which was successful for a bumblebee but time consuming on larger moth scans.

(4) approximates the ommatidia count and lens diameters with clusters. If the initial ODA count in step 3 fails to match clusters of both shells for spherical eyes, or if clusters are not detected by the algorithm for non-spherical eyes, inspection of centers superimposed on the 2D histograms can determine the best count. The distance between adjacent centroids approximates lens diameter. The ideal ommatidial axis is derived from planes formed by triplets of centers near the cluster, and we approximate the surface normal by averaging the normal vector for each plane. Singular value decomposition finds the longest semi-axis of the ellipsoid of a cluster to estimate the anatomical ommatidial axis. The angular difference between ideal and anatomical axes estimates anatomical skewness.

Ideally, anatomical axes of neighboring ommatidia would yield reliable IO angles, but results were highly variable. Especially in the bee scan, where angles were sometimes negative, the small cluster length compared to the intersection distance magnified the effect of angular deviations. While greater resolution, or using other structures to extend approximations closer to the intersection, could improve accuracy, we approximated anatomical IO angles by partitioning coordinates into evenly spaced vertical and horizontal sections (Figure 4 D), in which we projected clusters onto a parallel plane. For instance, for vertical sections, all clusters within a range of x values are considered and the 2D clusters formed by y and z values determine the vertical angle component. Nonlinear least squares regression fits a polynomial function of degree between 2 and 5, accepting higher degrees only when they reduce the sum of the squared residuals by at least 5%, and assuming IO angles are positive. This repeats independently for each vertical and horizontal section. The process approximates a horizontal and vertical subtended angle for each cluster pair and calculates the total angle as their hypotenuse. We call this hypotenuse the anatomical IO angle. While this method assumes one regression function per section, it allows different regression models per section and independent approximations for horizontal and vertical IO angles across the eye (Stavenga 1979). In addition, by keeping track of cluster pair orientation along the eye surface, we can calculate horizontal and vertical IO angles using the two-dimensional lattice proposed by Stavenga (1979; Figure 6C).

Finally, the program generates two spreadsheets: (1) for each crystalline cone cluster, the Cartesian and spherical coordinates of the centroid, the number and location of the points within its cluster, the

approximate lens diameter, and the ideal and anatomical axis direction vectors are saved per row; and (2) for each pair of adjacent crystalline cones, the cones' indexes from spreadsheet 1, the center coordinates for the two cones, the resulting orientation in polar coordinates, and the anatomical IO angle between the two are saved per row. These allow approximations of how spatial acuity, optical sensitivity, and the eye parameter (Snyder 1979) vary across the eye (Taylor et al. 2018). The full code for measuring ommatidia with µCT is available at www.github.com/jpcurrea/compound_eye_tools/, where you can download the Python package and basic examples on how to use it.

Results

Microscope Images

We tested the ODA on images of flattened eye molds of six ants from 5 different species (Figure 5A). Automated counts were on average 97% (95.6 – 98.7%) of those taken by hand and they shared a strong and significant correlation (r=.99, df=4, p□.001). The automated lens diameters were on average 99% (92.1 – 106.7%) of those taken by hand and also shared a strong and significant correlation (r=.82, df=4, p=.02).

We also tested microscope images of the eyes of 39 fruit flies (*D. melanogaster*; Figure 5B and C), to determine performance on direct images and comparisons within a species. Automated counts shared a strong and significant correlation with manual counts (r = .93, df = 37, p □ .001). Automated counts were 845 ± 87 (mean±standard deviation) while hand counts were 810 ± 76, with automated counts equalling 104 ± 4% of those taken by hand. Though the difference in counts was not significant (t = 1.8, df = 37, p = 0.07), automated counts may exceed the hand counts because of partial ommatidia that were excluded during the manual counting process but not the algorithm. Automated diameters also shared a strong and significant correlation with manual diameters (r = .82, df = 37, p □ .001). Automated diameters were 16.3 ± 1μm while manual diameters were 15.6 ± .8μm, with automated diameters equaling 105 ± 3% of those taken by hand and is close to the 16μm taken previously (Franceschini 1972). Automatic diameters were greater (t = 4, df = 37, p < .001) possibly because manual calculations were averaged over several ommatidia in a row, which assumed straight, regular alignment. Facets actually curve slightly with the curvature of the eye, and can be interrupted by lattice abnormalities (Ready, Hanson, and Benzer 1976). However, lattice irregularities do not affect automatic diameter measurements as they are individual, and should equal at least those taken by averaging over a straight distance.

μCT

We tested ODA-3D on eye scans of two moth species (*M. sexta* and *D. elpenor*) that we collected, and one bumblebee (*B. terrestris*) used in Taylor et al. (2018; Figure 6). We additionally tested methods for non-spherical eyes on the bumblebee scan (Figure 7), including for features of an oval eye, regional changes in aperture and anatomical IO angle, and projecting onto world-referenced coordinates.

The 2D histograms and the superimposed ommatidial centers suggested that the first count was more accurate for *M. sexta* while the second count was more accurate for *D. elpenor*. This was because of substantial noise around the eye boundary in *D. elpenor* that we failed to remove in the prefilter stage. For *B. terrestris*, though the first count was more accurate than the second, it still missed many ommatidia visible in the dorsal region of the bumblebee eye maps of Figures 4 and 6. This was mostly due to differential exposure across the eye, resulting in many crystalline cones that were excluded at the pre-filter stage. As a result, our ommatidia counts were comparable to previous counts in the literature for the moths but not the bumblebee. The first and second counts were 103 – 108% and 93 – 98% of previous measurements for *M. sexta* (Stöckl, O'Carroll, and Warrant 2017; White 2003), 120% and 106% for *D. elpenor* (Stöckl et al. 2017), and, for *B. terrestris*, 85% and 64% of both the density-based count of the same scan (Taylor et al. 2018) and previous manual counts for conspecific worker bees (Streinzer and Spaethe 2014). These ommatidia had diameters that were highly consistent with measurements in the literature: 96 – 108 % for *M. sexta* (Stöckl et al. 2017; Theobald, Warrant, and O'Carroll 2010; White 2003), 99 – 103% for *D. elpenor* (Stöckl et al. 2017; Theobald et al. 2010), and despite missing a large subsample of ommatidia, 102 – 104% for *B. terrestris* (Streinzer and Spaethe 2014; Taylor et al. 2018).

Both moth eyes showed ommatidial axes with minor skew from spherical alignment, potentially due to error estimating axes, or eye deformations during µCT preparations. The bee, however, showed axes with substantial skew, consistent with previous anatomical measurements (Baumgärtner 1928). Skew geometrically reduces effective lens diameter by the cosine of skew angle, and further still by refraction of the image space (Stavenga 1979). The adjustment without accounting for refraction produced marginal reductions for the spherical eyes: 0.5% in *M.sexta* and 0.7% in *D. elpenor*, but more substantial reduction for the oval eye: 12.7% in *B. terrestris*. The spherical approximations for IO angle were close to anatomical IO angle in moth eyes but not the bumblebee eye: 106% in *M. sexta*, 85% in *D. elpenor*, and 32% in *B. terrestris*. Likewise, anatomical IO angles were consistent with previous measurements in the literature for moths but less for the bumblebee: 92 – 97% for the spherical and 98 – 103% for the anatomical approximation in *M. sexta*, (Stöckl et al. 2017; Theobald et al. 2010), 97 – 113% for the spherical and 114 – 133% for the anatomical approximation in *D. elpenor* (Stöckl et al. 2017; Theobald et al. 2010), but 39 – 46% for the spherical and 121 – 143% for the anatomical approximation in *B. terrestris* (Spaethe 2003; Taylor et al. 2018).

In bees, spherical coordinates largely account for vertical axis curvature, but vastly underestimated horizontal curvature. To better characterize their visual field, we projected the ommatidial axes onto a

sphere outside of the eye, much like the world-referenced projection of Taylor et al. (2018; Figure 7C). However, instead of using the center of the head as our center, we used the center found in step B of ODA-3D, which is near but not exactly the center of the head. We chose a radius of 10 cm based on visual fixation behavior (Wehner and Flatt 1977). This world-referenced visual field has a FOV of about 140° horizontally and 140° vertically, agreeing exactly with previous measurements on the same scan that did not account for skewness (Taylor et al. 2018).

Oval Eye Properties

The bee eye is a non-spherical, oval eye, in which ommatidial axes intersect at different points for horizontal and vertical IO pairs (I_h and I_v in Figure 6C). Anatomical IO angles therefore should be separated into independent horizontal and vertical components ($\Delta\varphi_h$ and $\Delta\varphi_v$ in Figure 6C). In an oval eye: (1) the horizontal angle for horizontal IO pairs (0° orientation) is $2\Delta\varphi_h$ while the vertical angle is 0; (2) the horizontal and vertical angles for diagonal IO pairs (± 60° orientations) are $\Delta\varphi_h^2$ and $\Delta\varphi_v$; and (3) the proportion $\Delta\varphi_v / \Delta\varphi_h$ is $1/\sqrt{3}$ (Stavenga 1979). Our bee IO pair orientations followed a trimodal distribution with modes at -59°, 0°, and 61° (K Means algorithm with 3 means; N = 11,626, mean distance = 12°). We selected IO pairs within 15° of centroids to accurately measure horizontal and vertical angles (Figure 7A). The bee fits several oval eye predictions: (1) horizontal angle for horizontal IO pairs, 2.94°, is nearly twice horizontal angle for diagonal pairs, 1.90° + 1.36° = 3.26° while vertical angle, 0.08°, is close to 0; and (2) the vertical angles for diagonal IO pairs, .97° and .98°, are nearly equal. However, the horizontal angles for diagonal IO pairs, 1.90° and 1.36°, which should be equal, differ by about 28%.

By combining the horizontal angle of diagonal pairs and half the horizontal angle of horizontal pairs, we approximated the horizontal anatomical IO angle component, $\Delta\varphi_h = 1.48 \pm .88°$ (N = 7,503). This is close to the range of 1.8° – 3.3° measured previously (Spaethe 2003). By combining the vertical angles of diagonal pairs we approximate $\Delta\varphi_v = .95 \pm 0.60°$ (N = 4,828), which is within the range of 0.6° – 1.4° measured in Spaethe (2003). Using these two anatomical IO angle components, the total anatomical IO angle $\Delta\varphi = 1.76°$, is closer to the previous measurements of 1.6° and 1.9° mentioned above. Also, the proportion $\Delta\varphi_v / \Delta\varphi_h = .64$ is close to $1/\sqrt{3} = 0.58$, as predicted for an oval eye.

Interestingly, the anatomical IO angle components varied with elevation and azimuth (Figure 7B and C), which we binned into 15° intervals. $\Delta\varphi_v$ decreases by .3° horizontally from -37.5° azimuth to 7.5° azimuth (r = -.14, df = 2174, p □ 0.001) and then remains relatively constant up to 37.5° azimuth (r =

0.01, df = 1,414, p = 0.60; Figure B, top left). To our knowledge, this has not been measured previously but is consistent with the observation that the greatest overall acuity is in the central visual field (Baumgärtner 1928).

Vertically, $\Delta\varphi_v$ decreases by 1.3° from -67.5° to 22.5° elevation (r = -0.53, df = 4870, p □ 0.001) and then increases by .7° up to 52.5° elevation (r = 0.29, df = 2207, p □ 0.001; Figure B, top right). This agrees with previous measurements showing a decrease from about 2.4° ventrally to about 1° centrally followed by a gradual increase to about 2° dorsally. However, the previous measurement found a dramatic increase to 4° at the dorsal extreme (Baumgärtner 1928), which we did not measure. This is likely due to technical differences: their bee species is unspecified, their specimen may be smaller and thus have a larger $\Delta\varphi_v$ minimum than ours, and our eye scan lacks a substantial dorsal portion where they measured most of the increase (Baumgärtner 1928).

Horizontally, $\Delta\varphi_h$ decreases by 0.8° from -67.5° to -22.5° azimuth (r = -0.03, df = 6295, p < 0.01). This differs from the previous measurements taken on the same scan, which found that the anatomical IO angle increases from about 1.26° to 1.90° from the lateral to central eye with a strong positive correlation (r = 0.50, df = 3,471, p □ 0.001; Taylor et al., 2018). This is likely because the previous measurements did not account for skewness, which we find increases laterally, and partially explains why our anatomical IO angle measurement exceeds theirs by about 0.16°. Vertically, $\Delta\varphi_h$ decreases by .6° from -52.5° to 7.5° elevation, with an insignificant correlation (r = 0.03, df = 4,750, p = 0.06; Figure 7B, bottom right).

Adjusted lens diameter also varied with azimuth and elevation. Horizontally, it increases by 4 µm from -37.5° to 37.5° azimuth (r = 0.28, df = 3,542, p □ 0.001; Figure 7 B, bottom left, blue). The correlation largely reduces for absolute lens diameter (r = 0.09, df = 3,542, p □ 0.001; Figure 7B, bottom left, blue dashed line). Likewise, adjusted lens diameter increases vertically by 5 µm from -67.5° to 7.5° azimuth (r = 0.25, df = 1,845, p □ 0.001; Figure 7 B, top right, blue) while absolute lens diameter remains constant (r = -0.01, df = 3,542, p = 0.8; Figure 7B, top right, blue dashed line).

Skewness always reduces sensitivity but can lead to FOV and IO angle tradeoffs. In this eye, adjusted lens diameter, and consequently sensitivity, increases from the lateral to central visual field while vertical spatial acuity is highest near the center. Similarly, adjusted lens diameter, and consequently sensitivity, increases from the ventral to dorsal visual field. This results in high sensitivity and vertical spatial acuity near the central visual field at the expense of FOV, and greater FOV laterally and ventrally at the expense of sensitivity and vertical spatial acuity.

During visual fixation, bees incline their dorsal-ventral axis to 70° (Wehner and Flatt 1977), adjusting our elevation parameter by -20°, which appears to direct the region of optimal sensitivity and acuity (0° azimuth, 20° elevation) towards visual targets. Binocular overlap also occurs in the dorsomedial region with high vertical spatial acuity (Taylor et al. 2018). Similar tradeoffs are found in many other apposition eyes, but usually coincide with visible changes in diameter and curvature. In bees, though, the changes are not reflected in absolute lens diameters or IO angles that do not account for skewness, and were revealed only by analyzing skewness, which highlights both the flexibility gained by skewing ommatidia and its deceptive nature.

Discussion

Our methods successfully automate the estimation of multiple visual parameters of compound eyes. We tested compound eye images with the ODA, which filters frequencies based on the hexagonal arrangement of most ommatidia, and applies a local maximum detector to identify their centers. The ODA calculated ommatidial count and lens diameter from different media (eye molds, microscope images, and µCT scans), taxa (ants, flies, moths, and a bee), sizes (hundreds to tens of thousands of ommatidia), and eye type (apposition, neural superposition, and optical superposition). In all cases, measurements provided by the program matched with manual measurements on the same data, previous measurements in the literature, or both. Ommatidial counts were accurate, with an average proportion across all tested species of 93 – 102% (mean of low means – mean of high means%) of previous or manual measurements. Ommatidial diameters were even more accurate, with an average proportion across all tested species of 100.2 – 103.4% of previous or manual measurements.

The ODA-3D, which integrated the ODA into a µCT pipeline, proved successful on scans of two spherical moth eyes (*D. elpenor* and *M. sexta*) and one oval bee eye (*B. terrestris*). In addition to counts and diameters, ODA-3D estimated anatomical IO angles, FOV, and skewness, from which we calculated adjusted lens diameters to approximate the optical effects of skew. Skewness angles were insignificant in moth eyes, which generally require approximate spheracity for proper optical superposition. However the oval bumblebee eye showed significant skewness angles, implying reduced optical sensitivity. Again, estimates were consistent with manual measurements on the same data, previous measurements in the literature, or both. High resolution 3D data additionally offered world-referenced coordinates and regional measurements across the visual field. We found regional changes in skewness, vertical spatial acuity, and sensitivity as well as regional three-way tradeoffs between acuity, FOV, and sensitivity caused by skewness. Traditional methods, such as histological sections,

make it challenging to measure IO angles oriented along a perpendicular axis, where it is more efficient to measure multiple IO angles parallel to the sectioning plane than individual IO angles perpendicularly along many sections. With a 3D dataset the two are equally difficult, and across the bee eye we were able to measure horizontal resolution increasing vertically and vertical resolution increasing horizontally from the peripheral to the central visual field. As far as we know, this has not been measured previously, though it is consistent with previous measurements showing the greatest resolution in the central visual field (Baumgärtner 1928).

The great eye size range between and among invertebrate species (Casares and McGregor 2020; Currea et al. 2018; Gaspar et al. 2019; Land 1997; Land and Nilsson 2012; Shingleton et al. 2007), makes compound eyes ideal for studying environmental reaction norms and allometry. Little allometry research deals with compound eyes, and instead favors organs easily measured in one or two dimensions (McDonald et al. 2018; Shingleton et al. 2007; Shingleton, Mirth, and Bates 2008). By automating the more tedious tasks of characterizing compound eyes, our programs should help with this challenge. For instance, ODA counts and diameters allow total cell count approximations and correspond to the independent effects of cellular proliferation and growth during eye development. Further, our program facilitates measuring allometry of visual performance, addressing the environmental reaction norms of the anatomical determinants of vision. Further, progress in understanding fruit fly eye development (*D. melanogaster*; Callier and Nijhout 2013; Casares and McGregor 2020; Gaspar et al. 2019; Ready et al. 1976), makes compound eyes ideal for assessing principles of eye development across different taxa (Casares and McGregor 2020; Friedrich 2003; Harzsch and Hafner 2006). And because optics are the first limit to incoming visual information (Land 1997; Stavenga 1979), they inform electrophysiological and behavioral data to infer intermediate neural processing (Currea et al. 2018; Gonzalez-Bellido, Wardill, and Juusola 2011; Juusola et al. 2017; Land and Nilsson 2012; Theobald et al. 2010; Wardill et al. 2017; Warrant 1999).

Our programs have some known limitations. Images for the ODA require sufficient resolution to properly detect ommatidia. For regular images, pixel length must be at most half the smallest ommatidial diameter. For µCT, if individual crystalline cones cannot be resolved at each layer, they are likely indiscriminable to the ODA. Further, some species, preparations, and scanning procedures, capture better contrast between crystalline cones and other structures while avoiding structural damage to the specimen. For example, *M. sexta* crystalline cones contrasted sharply with the background scan when prefiltered with just the threshold function. *D. elpenor*, however, had additional noise outside of the eye, and *B. terrestris* had uneven exposure, altering density measurements across locations in the

scan and ultimately forcing omission of data. This may be an unintentional consequence of the contrast enhancing property of a synchrotron light source (Baird and Taylor 2017).

Ultimately, anatomical measurements cannot replace optical techniques in measuring compound eye optics (Stavenga 1979; Taylor et al. 2018). Light passing through an eye refracts depending on the incident angle and index of refraction (Stavenga 1979). But our approximations used only incident angle, so our measurements of the aperture-diminishing effect of skewness represent lower bounds, and our measurements of IO angles are *anatomical*, not functional IO angles. Though skewness can be somewhat corrected for, nothing can match optical techniques (Stavenga 1979; Taylor et al. 2018).

Future work will be needed to understand the limitations of both the ODA and ODA-3D. Because the ODA depends on spatial frequencies corresponding inversely to the ommatidial diameter, an eye with a wide range of diameters may not work, and the ODA should be tested on eyes containing acute or sensitive zones, such as the robberfly (Wardill et al. 2017) and lattices with transitioning arrangements, such as hexagon to square in houseflies (Stavenga 1975) and male blowflies (Smith et al. 2015). Likewise, the ODA-3D should be tested on non-spherical non-oval eyes. While our program appropriately measured anatomical IO angles across the bumblebee's oval eye and actually corroborated its oval eye properties, it may not work when IO angles change dramatically like in the robberfly (Wardill et al. 2017). Finally, the ODA-3D should be tested on non-insect arthropods.

Conclusion

Compound eyes are the most common eye type on Earth, found in nearly every ecological habitat and visual environment, and varying widely in size, shape, and architecture. Because they are diverse, ubiquitous, and subject to heavy selection pressure, they are crucial to understanding the evolution of vision. Our programs contribute to this effort and are open source, easy to install, easy to incorporate into custom pipelines, and downloadable as Python modules (ODA: https://github.com/jpcurrea/fly_eye; ODA-3D: https://github.com/jpcurrea/compound_eye_tools). By successfully measuring parameters from a wide range of eye shapes and sizes, they should facilitate the study of the development, evolution, and ecology of visual systems in non-model organisms.

Contribution: JC: Conceptualization, Methodology, Software, Visualization, Writing- Original Draft. YS: Conceptualization, Methodology, Writing- Review and Editing, Data Collection and Curation. JT: Conceptualization, Methodology, Writing- Review and Editing, Supervision, Funding acquisition. AK: Conceptualization, Methodology, Writing- Review and Editing, Funding acquisition.

Funding: This research was supported by grants from the National Science Foundation: IOS-1750833 to JT, BCS-1525371 to JC, DEB-1557007 to AYK and JT and IOS-1920895 to AYK. The content is solely the responsibility of the authors and does not necessarily represent the official views of the National Institutes of Health or the National Science Foundation.

Acknowledgements: We thank members of the Kawahara Lab at the Florida Museum of Natural History, McGuire Center for Lepidoptera and Biodiversity, for raising and vouchering moth specimens. The University of Florida CT facility is thanked for helping acquiring the *M. sexta* CT scan, and Kelly Dexter for help with sample staining. We thank Deborah Glass and Ian Kitching from the Natural History Museum of London for help with the CT procedure and sharing the *D. elpenor* CT scan, which study was funded by NERC grant number NE/P003915/1 to IJK. Gavin Taylor and Emily Baird shared their CT scans of *B. terrestris*. Michael Reisser and Arthur Zhao provided valuable discussions regarding the uCT pipeline.

References

Baird, Emily, and Gavin Taylor. 2017. "X-Ray Micro Computed-Tomography." *Current Biology* 27(8):R289–91. doi: 10.1016/j.cub.2017.01.066.

Baumgärtner, Herbert. 1928. "Der Formensinn Und Die Sehschärfe Der Bienen." *Zeitschrift Für Vergleichende Physiologie* 7(1):56–143.

Brodrick, Emelie A., Nicholas W. Roberts, Lauren Sumner□Rooney, Christian M. Schlepütz, and Martin J. How. 2020. "Light Adaptation Mechanisms in the Eye of the Fiddler Crab *Afruca Tangeri*." *Journal of Comparative Neurology* cne.24973. doi: 10.1002/cne.24973.

Buser, T. J., O. F. Boyd, Á. Cortés, C. M. Donatelli, M. A. Kolmann, J. L. Luparell, J. A. Pfeiffenberger, B. L. Sidlauskas, and A. P. Summers. 2020. "The Natural Historian's Guide to the CT Galaxy: Step-by-Step Instructions for Preparing and Analyzing Computed Tomographic (CT) Data Using Cross-Platform, Open Access Software." *Integrative Organismal Biology* 2(obaa009). doi: 10.1093/iob/obaa009.

Callier, Viviane, and H. Frederik Nijhout. 2013. "Body Size Determination in Insects: A Review and Synthesis of Size- and Brain-Dependent and Independent Mechanisms." *Biological Reviews* 88(4):944–54. doi: 10.1111/brv.12033.

Casares, Fernando, and Alistair P. McGregor. 2020. "The Evolution and Development of Eye Size in Flies." *WIREs Developmental Biology* n/a(n/a):e380. doi: 10.1002/wdev.380.

Cronin, Thomas W., Sönke Johnsen, N. Justin Marshall, and Eric J. Warrant. 2014. *Visual Ecology*. Princeton University Press.

Currea, John P., Joshua L. Smith, and Jamie C. Theobald. 2018. "Small Fruit Flies Sacrifice Temporal Acuity to Maintain Contrast Sensitivity." *Vision Research* 149:1–8. doi: 10.1016/j.visres.2018.05.007.

Diez-Hermano, Sergio, Jorge Valero, Cristina Rueda, Maria D. Ganfornina, and Diego Sanchez. 2015. "An Automated Image Analysis Method to Measure Regularity in Biological Patterns: A Case Study in a Drosophila Neurodegenerative Model." *Molecular Neurodegeneration* 10(1):9. doi: 10.1186/s13024-015-0005-z.

Franceschini, N. 1972. "Pupil and Pseudopupil in the Compound Eye of Drosophila." Pp. 75–82 in *Information Processing in the Visual Systems of Anthropods*, edited by R. Wehner. Berlin, Heidelberg: Springer Berlin Heidelberg.

Friedrich, Markus. 2003. "Evolution of Insect Eye Development: First Insights from Fruit Fly, Grasshopper and Flour Beetle." *Integrative and Comparative Biology* 43(4):508–21. doi: 10.1093/icb/43.4.508.

Gaspar, Pedro, Saad Arif, Lauren Sumner-Rooney, Maike Kittelmann, David L. Stern, Maria D. S. Nunes, and Alistair P. McGregor. 2019. "Characterisation of the Genetic Architecture Underlying Eye Size Variation within Drosophila Melanogaster and Drosophila Simulans." *BioRxiv* 555698. doi: 10.1101/555698.

Gonzalez-Bellido, Paloma T., Trevor J. Wardill, and Mikko Juusola. 2011. "Compound Eyes and Retinal Information Processing in Miniature Dipteran Species Match Their Specific Ecological Demands." *Proceedings of the National Academy of Sciences* 108(10):4224–29. doi: 10.1073/pnas.1014438108.

Harzsch, Steffen, and Gary Hafner. 2006. "Evolution of Eye Development in Arthropods: Phylogenetic Aspects." *Arthropod Structure & Development* 35(4):319–40. doi: 10.1016/j.asd.2006.08.009.

Holthuis, Lipke B. 1991. "Marine Species Identification Portal□: Green Rock Lobster - Jasus Verreauxi." *Food and Agriculture Organization of the United Nations* 13(125).

Huber, John, and John Noyes. 2013. "A New Genus and Species of Fairyfly, Tinkerbella Nana (Hymenoptera, Mymaridae), with Comments on Its Sister Genus Kikiki, and Discussion on

Small Size Limits in Arthropods." *Journal of Hymenoptera Research* 32:17–44. doi: 10.3897/jhr.32.4663.
Huber, John T., and John W. Beardsley. 2000. "A New Genus of Fairyfly, Kikiki, from the Hawaiian Islands (Hymenoptera: Mymaridae)." *Hawaiian Entomological Society*.
Iyer, Janani, Qingyu Wang, Thanh Le, Lucilla Pizzo, Sebastian Grönke, Surendra S. Ambegaokar, Yuzuru Imai, Ashutosh Srivastava, Beatriz Llamusí Troisí, and Graeme Mardon. 2016. "Quantitative Assessment of Eye Phenotypes for Functional Genetic Studies Using Drosophila Melanogaster." *G3: Genes, Genomes, Genetics* 6(5):1427–37.
Juusola, Mikko, An Dau, Zhuoyi Song, Narendra Solanki, Diana Rien, David Jaciuch, Sidhartha Anil Dongre, Florence Blanchard, Gonzalo G. de Polavieja, Roger C. Hardie, and Jouni Takalo. 2017. "Microsaccadic Sampling of Moving Image Information Provides Drosophila Hyperacute Vision." *ELife* 6. doi: 10.7554/eLife.26117.
Kensler, Craig B. 1967. "The Distribution of Spiny Lobsters in New Zealand Waters (Crustacea: Decapoda: Palinuridae)." *New Zealand Journal of Marine and Freshwater Research* 1(4):412–20. doi: 10.1080/00288330.1967.9515216.
Land, Michael F. 1997. "Visual Acuity in Insects." *Annual Review of Entomology* 42(1):147–77.
Land, Michael F., and Dan-Eric Nilsson. 2012. *Animal Eyes*. OUP Oxford.
McDonald, Jeanne M. C., Shampa M. Ghosh, Samuel J. L. Gascoigne, and Alexander W. Shingleton. 2018. "Plasticity Through Canalization: The Contrasting Effect of Temperature on Trait Size and Growth in Drosophila." *Frontiers in Cell and Developmental Biology* 6:156. doi: 10.3389/fcell.2018.00156.
Mohrbeck, Inga, Pedro Martínez Arbizu, and Thomas Glatzel. 2010. "Tantulocarida (Crustacea) from the Southern Ocean Deep Sea, and the Description of Three New Species of Tantulacus Huys, Andersen & Kristensen, 1992." *Systematic Parasitology* 77(2):131–51. doi: 10.1007/s11230-010-9260-0.
Palavalli-Nettimi, Ravindra, and Ajay Narendra. 2018. "Miniaturisation Decreases Visual Navigational Competence in Ants." *Journal of Experimental Biology* 221(7):jeb177238.
Palavalli-Nettimi, Ravindra, Yuri Ogawa, Laura A. Ryan, Nathan S. Hart, and Ajay Narendra. 2019. "Miniaturisation Reduces Contrast Sensitivity and Spatial Resolving Power in Ants." *Journal of Experimental Biology* 222(12). doi: 10.1242/jeb.203018.
Ready, Donald F., Thomas E. Hanson, and Seymour Benzer. 1976. "Development of the Drosophila Retina, a Neurocrystalline Lattice." *Developmental Biology* 53(2):217–40. doi: 10.1016/0012-1606(76)90225-6.
Schramm, Bartosz W., Agnieszka Gudowska, Filip Kapustka, Anna Maria Labecka, Marcin Czarnoleski, and Jan Kozłowski. 2015. "Automated Measurement of Ommatidia in the Compound Eyes of Beetles." *BioTechniques* 59(2):99–101. doi: 10.2144/000114316.
Shingleton, Alexander W., W. Anthony Frankino, Thomas Flatt, H. Frederik Nijhout, and Douglas. J. Emlen. 2007. "Size and Shape: The Developmental Regulation of Static Allometry in Insects." *BioEssays* 29(6):536–48. doi: 10.1002/bies.20584.
Shingleton, Alexander W., Christen K. Mirth, and Peter W. Bates. 2008. "Developmental Model of Static Allometry in Holometabolous Insects." *Proceedings of the Royal Society of London B: Biological Sciences* 275(1645):1875–85. doi: 10.1098/rspb.2008.0227.
Smith, Dylan B., Galina Bernhardt, Nigel E. Raine, Richard L. Abel, Dan Sykes, Farah Ahmed, Inti Pedroso, and Richard J. Gill. 2016. "Exploring Miniature Insect Brains Using Micro-CT Scanning Techniques." *Scientific Reports* 6(1). doi: 10.1038/srep21768.
Smith, J. L., N. A. Palermo, J. C. Theobald, and J. D. Wells. 2015. "Body Size, Rather Than Male Eye Allometry, Explains Chrysomya Megacephala (Diptera: Calliphoridae) Activity in Low Light." *Journal of Insect Science* 15(1):133. doi: 10.1093/jisesa/iev114.
Snyder, Allan W. 1979. "Physics of Vision in Compound Eyes." Pp. 225–313 in *Comparative*

Physiology and Evolution of Vision in Invertebrates, *Handbook of Sensory Physiology*, edited by H. Autrum. Springer Berlin Heidelberg.
Snyder, Allan W., Simon B. Laughlin, and Doekele G. Stavenga. 1977. "Information Capacity of Eyes." *Vision Research* 17(10):1163–75. doi: 10.1016/0042-6989(77)90151-1.
Snyder, Allan W., Doekele G. Stavenga, and Simon B. Laughlin. 1977. "Spatial Information Capacity of Compound Eyes." *Journal of Comparative Physiology* 116(2):183–207.
Spaethe, J. 2003. "Interindividual Variation of Eye Optics and Single Object Resolution in Bumblebees." *Journal of Experimental Biology* 206(19):3447–53. doi: 10.1242/jeb.00570.
Stavenga, Doekele G. 1975. "The Neural Superposition Eye and Its Optical Demands." *Journal of Comparative Physiology? A* 102(4):297–304. doi: 10.1007/BF01464342.
Stavenga, Doekele G. 1979. "Pseudopupils of Compound Eyes." Pp. 357–439 in *Comparative Physiology and Evolution of Vision in Invertebrates*. Vol. 7 / 6 / 6 A, edited by H. Autrum. Berlin, Heidelberg: Springer Berlin Heidelberg.
Stöckl, A. L., D. O'Carroll, and E. J. Warrant. 2017. "Higher-Order Neural Processing Tunes Motion Neurons to Visual Ecology in Three Species of Hawkmoths." *Proceedings of the Royal Society B: Biological Sciences* 284(1857):20170880. doi: 10.1098/rspb.2017.0880.
Streinzer, Martin, and Johannes Spaethe. 2014. "Functional Morphology of the Visual System and Mating Strategies in Bumblebees (Hymenoptera, Apidae, *Bombus*): *Bombus* Compound Eye Morphology." *Zoological Journal of the Linnean Society* 170(4):735–47. doi: 10.1111/zoj.12117.
Taylor, Gavin J., Stephen A. Hall, Johan A. Gren, and Emily Baird. 2020. "Exploring the Visual World of Fossilized and Modern Fungus Gnat Eyes (Diptera: Keroplatidae) with X-Ray Microtomography." *Journal of The Royal Society Interface* 17(163):20190750. doi: 10.1098/rsif.2019.0750.
Taylor, Gavin J., Willi Ribi, Martin Bech, Andrew J. Bodey, Christoph Rau, Axel Steuwer, Eric J. Warrant, and Emily Baird. 2016. "The Dual Function of Orchid Bee Ocelli as Revealed by X-Ray Microtomography." *Current Biology* 26(10):1319–24. doi: 10.1016/j.cub.2016.03.038.
Taylor, Gavin J., Pierre Tichit, Marie D. Schmidt, Andrew J. Bodey, Christoph Rau, and Emily Baird. 2018. "Bumblebee Visual Allometry Results in Locally Improved Resolution and Globally Improved Sensitivity." *BioRxiv*. doi: 10.1101/380527.
Theobald, Jamie. 2017. "Optic Flow Induces Spatial Filtering in Fruit Flies." *Current Biology* 27(6):R212–13.
Theobald, Jamie C., Eric J. Warrant, and David C. O'Carroll. 2010. "Wide-Field Motion Tuning in Nocturnal Hawkmoths." *Proceedings of the Royal Society of London B: Biological Sciences* 277(1683):853–60. doi: 10.1098/rspb.2009.1677.
Vanhoutte, Kurt J. A., Kristel F. L. Michielsen, and Doekele G. Stavenga. 2003. "Analyzing the Reflections from Single Ommatidia in the Butterfly Compound Eye with Voronoi Diagrams." *Journal of Neuroscience Methods* 131(1):195–203. doi: 10.1016/j.jneumeth.2003.08.011.
Walker, Simon M., Daniel A. Schwyn, Rajmund Mokso, Martina Wicklein, Tonya Müller, Michael Doube, Marco Stampanoni, Holger G. Krapp, and Graham K. Taylor. 2014. "In Vivo Time-Resolved Microtomography Reveals the Mechanics of the Blowfly Flight Motor." *PLOS Biology* 12(3):e1001823. doi: 10.1371/journal.pbio.1001823.
Wardill, Trevor J., Samuel T. Fabian, Ann C. Pettigrew, Doekele G. Stavenga, Karin Nordström, and Paloma T. Gonzalez-Bellido. 2017. "A Novel Interception Strategy in a Miniature Robber Fly with Extreme Visual Acuity." *Current Biology* 27(6):854–59. doi: 10.1016/j.cub.2017.01.050.
Warrant, Eric J. 1999. "Seeing Better at Night: Life Style, Eye Design and the Optimum Strategy of Spatial and Temporal Summation." *Vision Research* 39(9):1611–30. doi: 10.1016/S0042-6989(98)00262-4.
Wehner, R., and I. Flatt. 1977. "Visual Fixation in Freely Flying Bees." *Zeitschrift Für Naturforschung*

C 32(5–6):469–72.
White, R. H. 2003. “The Retina of Manduca Sexta: Rhodopsin Expression, the Mosaic of Green-, Blue- and UV-Sensitive Photoreceptors, and Regional Specialization.” *Journal of Experimental Biology* 206(19):3337–48. doi: 10.1242/jeb.00571.
Woodman, Peter N., Amy M. Todd, and Brian E. Staveley. 2011. “Eyer: Automated Counting of Ommatidia Using Image Processing Techniques.” *Drosophila Information Service* 94:142.
Zhang, Zhi-Qiang. 2013. “Animal Biodiversity: An Update of Classification and Diversity in 2013. In□: Zhang, Z.-Q. (Ed.) Animal Biodiversity: An Outline of Higher-Level Classification and Survey of Taxonomic Richness (Addenda 2013).” *Zootaxa* 3703(1):5–11. doi: 10.11646/zootaxa.3703.1.3.

Figures

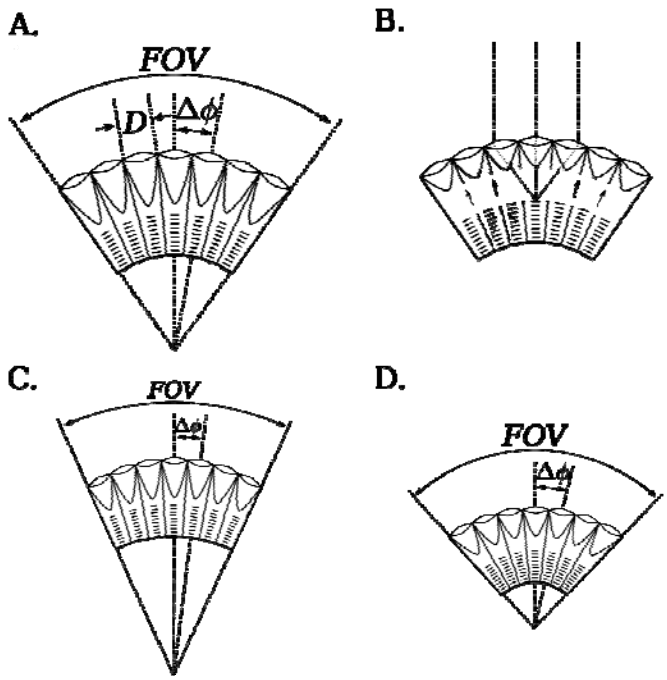

Figure 1: Diagrams of apposition and superposition eyes demonstrating the geometric tradeoffs between lens diameter (D), interommatidial angle (Δφ), and field of view (FOV) for spherical (A. and B.) and non-spherical eyes (C. and D.). **A.** In spherical apposition eyes, D directly determines sensitivity while Δφ inversely determines acuity. **B.** In superposition eyes, migrating pigment (indicated by the arrows) allows the ommatidia to share light, increasing the eye’s sensitivity. As a result, these eyes must adhere to a spherical design. **C-D.** In non-spherical eyes, the intersection of ommatidial axes differs from the center of curvature, with ommatidial axes askew from the surface of the eye. Consequently, FOV and Δφ are not externally measurable and the effect of D on sensitivity is reduced by greater angles of skewness. **C.** When the distance to the intersection is greater than the radius of curvature, FOV and Δφ decrease, increasing average spatial acuity by directing more ommatidia over a smaller total angle. **D.** Inversely, when the distance to the intersection is less than the radius of curvature, FOV and Δφ increase, decreasing average spatial acuity by directing fewer ommatidia over a smaller total angle. In both cases, optical sensitivity is lost because skewness reduces the effective aperture of the ommatidia.

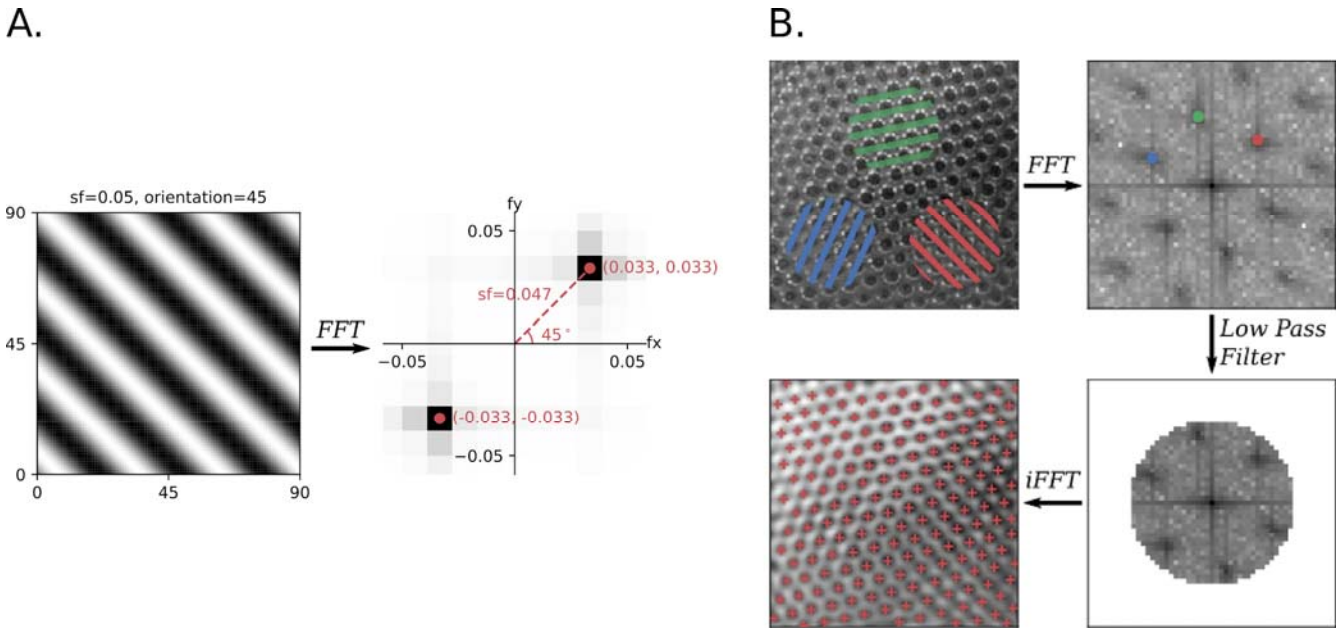

Figure 2: The ommatidia detecting algorithm (ODA) extracts periodic signals in a 2D image using the FFT. A. In the frequency domain of a 2D FFT, called the reciprocal space, gratings are represented by an x- and y-frequency. The polar coordinates represent visual properties of the corresponding grating. The radial distance is a grating's spatial frequency, with high frequencies farther from the origin. The polar angle is the grating's orientation , which is perpendicular to the grating's wavefront. Notice that the reciprocal space has local maxima (in red) approximately equal to the input grating parameters (polar angle=45° and radial distance=.047±.005). B. In a hexagonal lattice, there are three major axes (here in blue, green, and red). Each axis corresponds to a 2D spatial frequency (and it's negative), visible in the image's reciprocal space. The periodic nature of the axes results in harmonic frequencies. A low-pass filter returns a version of our original image primarily representing these three axes. The center of each ommatidium is found at the local maxima of the filtered image.

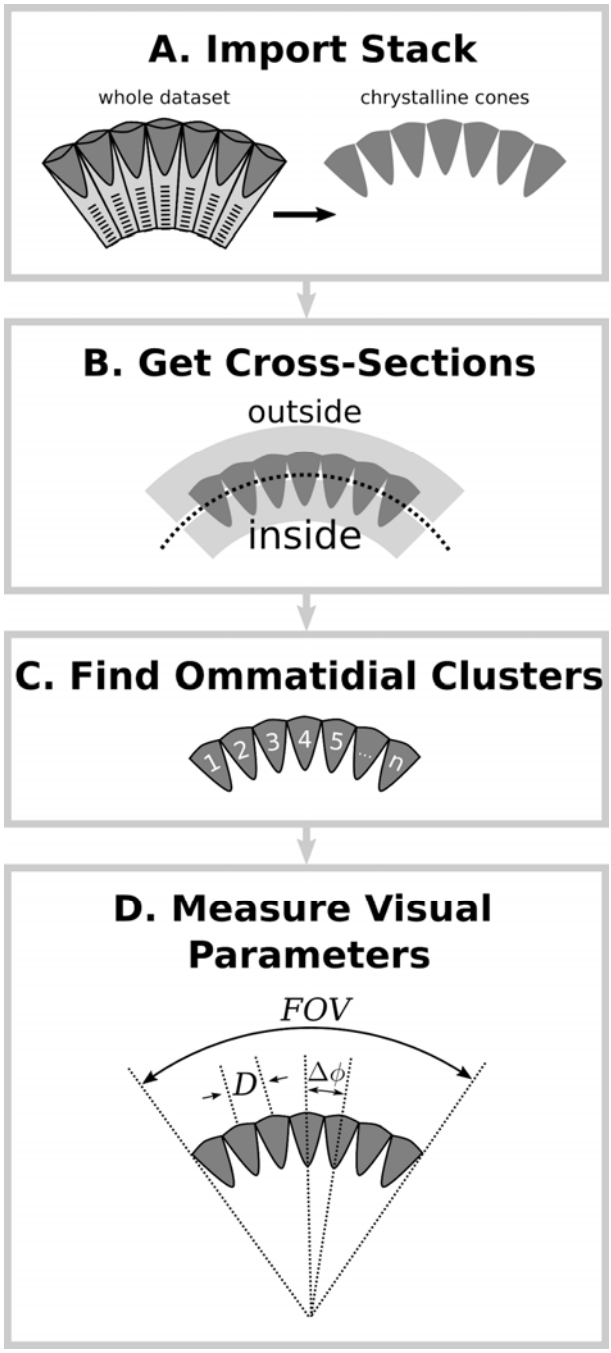

Figure 3: ODA-3D starts with an image stack, which may be pre-filtered and cleaned of unrelated structures. Then we filter the relevant density values and fit a surface to the coordinates, allowing us to split the points into two sets or cross sections, inside and outside the fitted surface. For each cross section, we generate spherically projected, rasterized images that are processed by the FFT method for locating ommatidia, yielding approximate centers for the ommatidia. With these centers, we can find the coordinate clusters corresponding to independent ommatidia and automatically measure eye parameters.

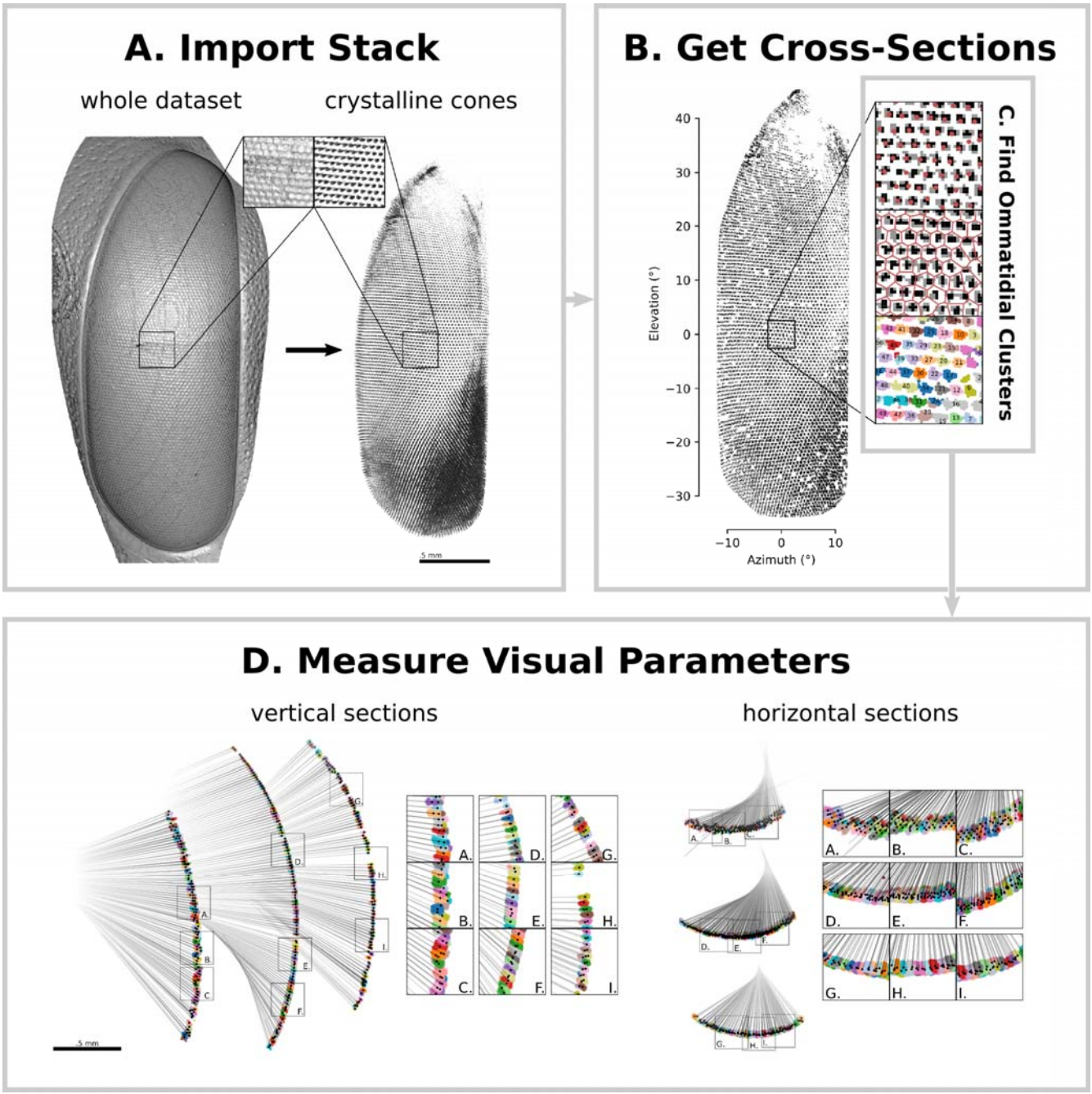

Figure 4: Checkpoints along ODA-3D for the bumblebee scan. **A. Import Stack**: The bumblebee ODA-3D pipeline started with an image stack that we pre-filtered and manually cleaned of unrelated structures. **B. Get Cross-Sections:** A surface was fitted to the coordinates identifying a cross-section of points within 50% of the residuals. We generated a spherically projected, 2D histogram of the crystalline cone coordinates (in grayscale). **C. Find Ommatidial Clusters**: The inset zooms into stages of applying the ODA to label individual crystalline cones. The ODA locates the cluster centers (red dots in *top*), allowing us to partition the coordinates based on their distance to those centers (boundaries indicated by the red lines in *middle*). Then we apply the spectral clustering algorithm to all of the 3D coordinates using the ommatidia count (*bottom*), finding the clusters approximating the individual crystalline cones (each colored and labelled separately in *bottom*). **D. Measure Visual Parameters:** Ommatidial diameter corresponds to the average distance between clusters and their adjacent neighbors. Ommatidial count corresponds to the number of clusters. For non-spherical eyes, we can partition the 3D coordinates into vertical (*left*) and horizontal (*right*) cross-sections in order to calculate independent vertical and horizontal anatomical IO angle components accounting for skewness in the ommatidial axes. The insets zoom into regions around the 25th, 50th, and 75th percentile ommatidia along the y-axis (*left*) and x-axis (*right*). Note: in **C** and **D** the different colors

signify different crystalline cone clusters. In **D**, the black lines follow the ommatidial axes and the black dots indicate the cluster centroids.

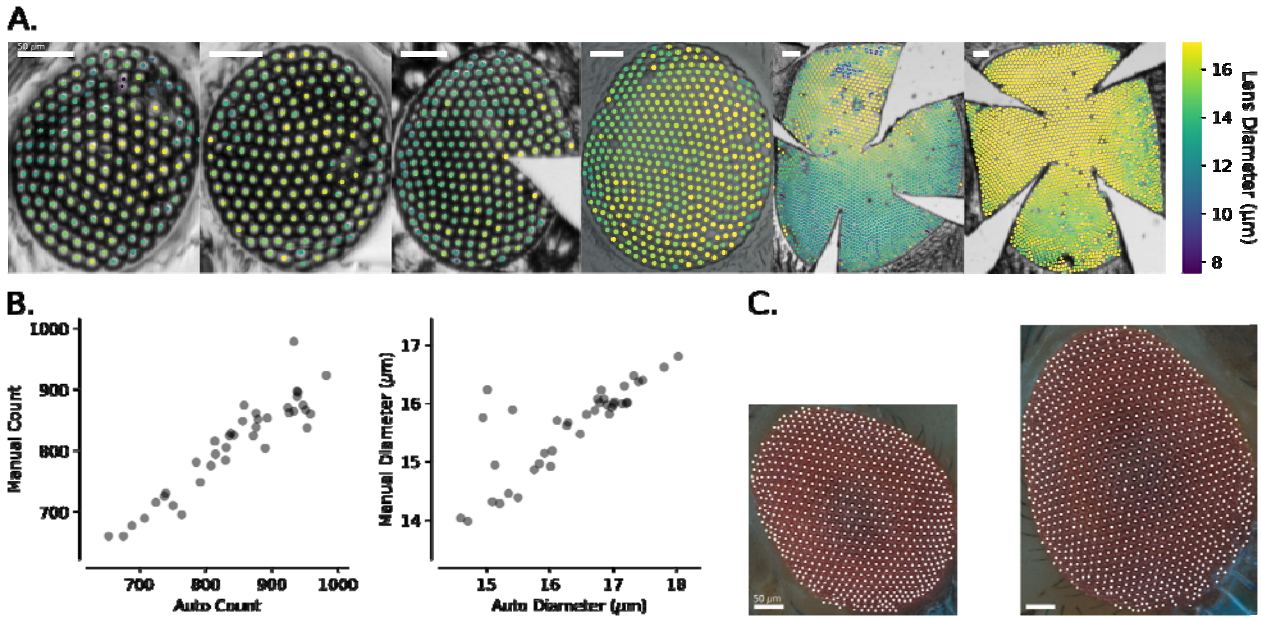

Figure 5: The ODA successfully approximated ommatidial counts and diameters when compared to manual measurements. **A.** When applied to 6 ant eye molds of 5 species ranging in overall size and lattice regularity, the automated counts were 97% and the diameters were 99% of those measured by hand. For each image, the program missed relatively few ommatidia and the lens diameter measurements were successful even when they varied substantially within an image (as in #5 from the left). Species from left to right: Notoncus ectatommoides, Notoncus ectatommoides, Rhytidoponera inornata, Camponotus aeneopilosus, Myrmecia nigrocincta, and Myrmecia tarsata. **B.** When applied to 39 microscope images of fruit fly eyes from the same species (D. melanogaster), the automated counts were 104% and the diameters were 105% of those measured by hand, with correlations of .93 and .82. **C.** Two example fruit fly eyes, one small and one large, with the automated ommatidia centers superimposed as white dots. Again, there were relatively low rates of false positives and negatives. Scale bars are 50µm.

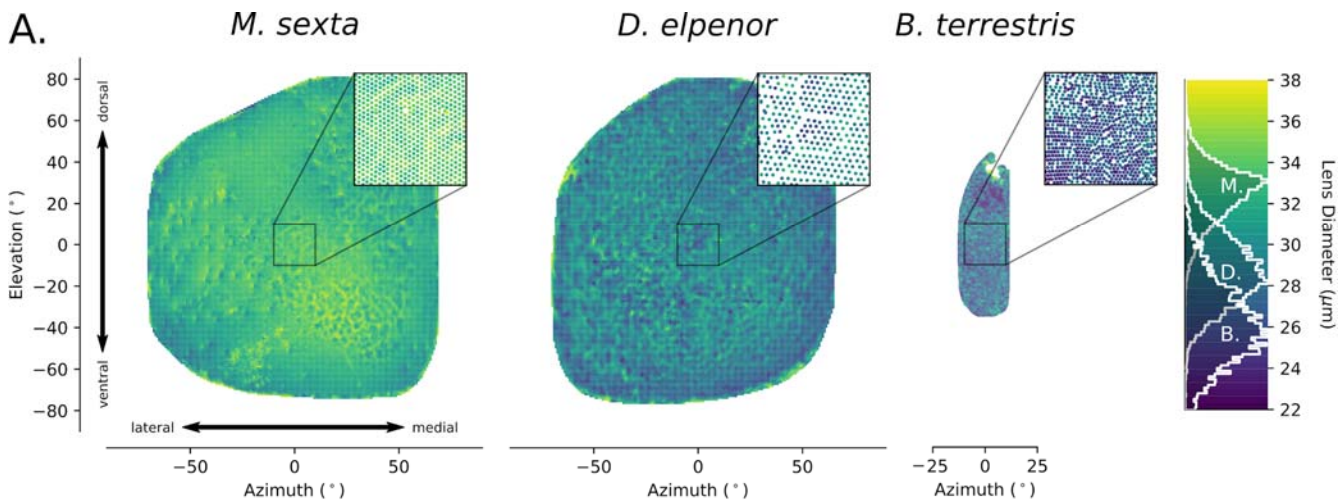

B.

	Species		
	M. sexta	*D. elpenor*	*B. terrestris*
Count	25159 – 27756	12172 – 13801	3562 – 4765
	27000 [a], 25641 [b]	11508 [b]	5597 [d], 5624 ±369 [e]
Lens Diameter (μm)	32.5 ±1.5	28.8 ±1.9	26.1 ±2.1
	30 [a], 31 [b], 34 [c]	28 [b], 29 [c]	25.6 ±2.5 [d], 25.1 ±1.9 [e]
Skewness (°)	5.7 (4.4)	6.6 (5.1)	29.2 (18.0)
			≤ 50 [f]
Adjusted Lens Diameter (μm)	32.2 ±1.6	28.4 ±1.9	22.1 ±3.7
Spherical IO Angle (°)	0.88 (.16)	1.27 (.35)	0.74 (.27)
Anatomical IO Angle (°)	0.94 (.33)	1.49 (.74)	2.29 (1.65)
	0.91 [b], 0.96 [c]	1.12 [b], 1.31 [c]	1.6 [d], 1.9 [g]

C.

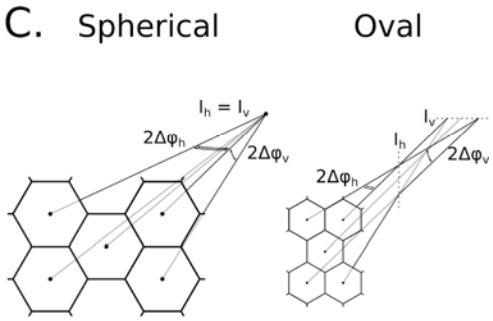

Figure 6: Comparing visual fields based on the spherical approximation. **A.** ODA-3D allows us to map the visual fields of our three specimens. Using their spherical projection, we map the azimuth (along the lateral-medial axis) and elevation (along the ventral-dorsal axis) angles of ommatidia and represent lens diameter with color. The colorbar to the right indicates lens diameter, and shows diameter histograms for each species in white. Insets zoom in on a 20°x20° region in the center of each eye, showing ommatidial lattices in more detail. Note that the spherical projection of the bee eye underestimates its visual field and is missing a portion dorsally, as explained in the text. **B.** Optical parameters for the three species are presented as a table. Values are mean ± s.d except for angular measurements, which show median (IQR). Comparable measurements from the literature are in grey below corresponding values. References are signified in superscript letters: [a] White (2003), [b] Stöckl et al. (2017), [c] Theobald et al.(2010), [d] Taylor et al. (2018), [e] Streinzer and Spaethe (2014), [f] Baumgärtner (1928), [g] Spaethe (2003). **C.** Adapted from Stavenga, 1979. Bee eyes are approximately oval, and, unlike spherical eyes, have different intersection points for horizontal (I_h) and vertical (I_v) ommatidial pairs corresponding to different IO angle components horizontally ($\Delta\varphi_h$) and vertically ($\Delta\varphi_v$). For oval eyes, the horizontal component of the IO angle of horizontal pairs (orientation=0°) is $2\Delta\varphi_h$ while the vertical component is ~0° and the horizontal component of diagonal pairs (orientation=±60°) is $\Delta\varphi_h$ while the vertical component is $\Delta\varphi_v$. Because the ommatidia form an approximately regular hexagonal lattice, $\Delta\varphi_v/\Delta\varphi_h = 1/\sqrt{3}$ for spherical eyes, and $\sqrt{3}$ for oval eyes.

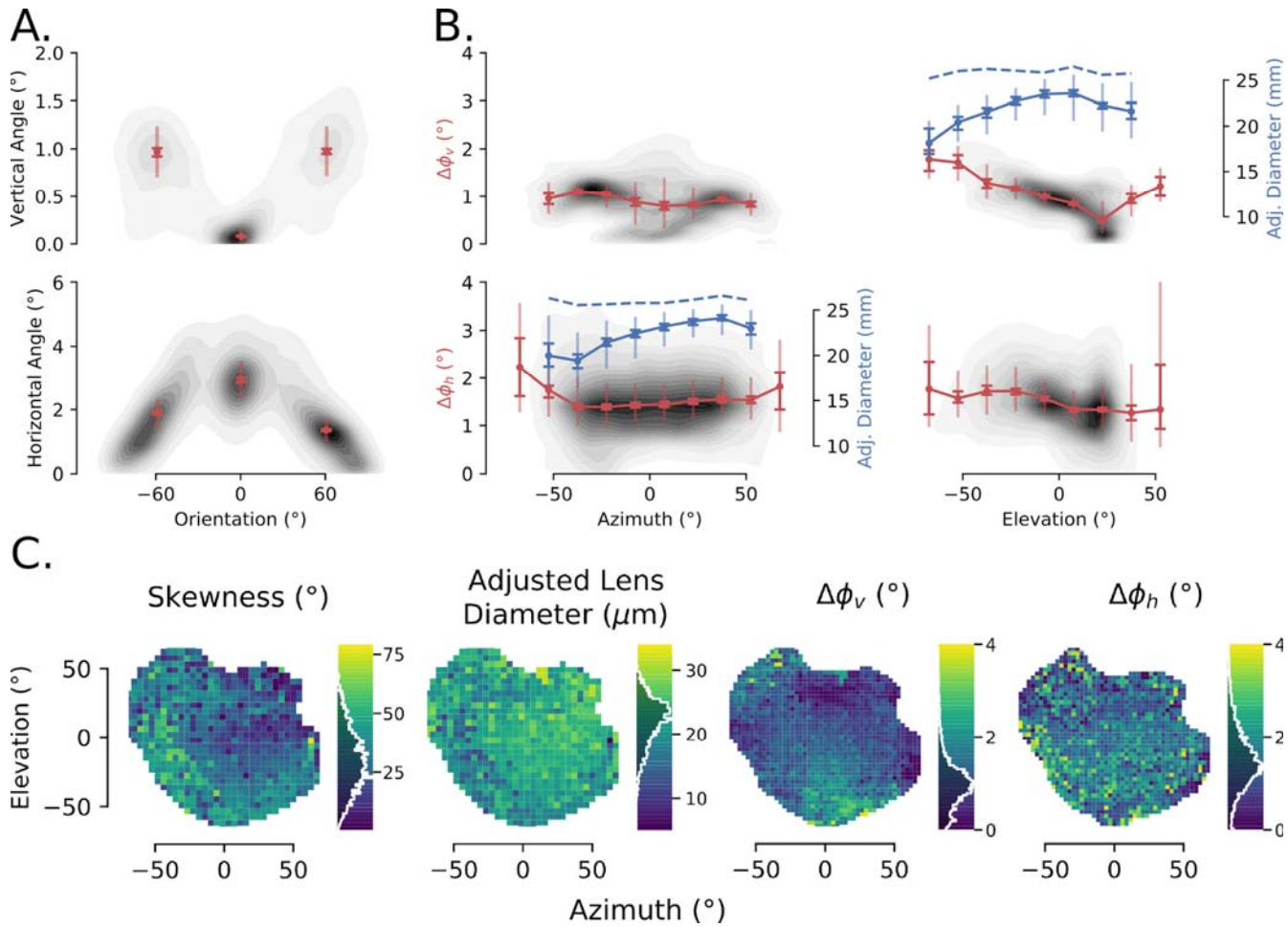

Figure 7: Mapping optical parameters onto the visual field of *B. terrestris*. **A**, **B.** Grayscale heatmaps indicate kernel density estimation of the entire dataset and red lines indicate statistics about surrounding clusters: the longer, half opacity lines indicate IQR, tick marks indicate the 99% CI of the median using bootstrapping, and points (often overlapping with the tick marks) indicate the median. Solid blue lines, ticks, and points indicate the median and IQR of adjusted lens diameters in the same way as red lines, and correspond to inserted axes on the right. Dashed blue lines indicate the median absolute lens diameters also corresponding to the axes on the right. **A.** The vertical and horizontal subtended angles of ommatidial pairs with respect to their orientation fit well into the oval eye lattice from Figure 6C. The pair orientations form a trimodal distribution with means close to ±60° (diagonal pairs) and 0° (horizontal pairs). Medians, IQRs, and 99% C.I.s are plotted for each orientation ±15°. **B.** Using the lattice described in Figure 6C, we convert the horizontal and vertical subtended angles into the horizontal and vertical IO angle components ($\Delta\varphi_h$ and $\Delta\varphi_v$) and plot them with respect to their azimuth and elevation positions on the projected visual field. C. Skewness varies systematically across the eye influencing adjusted lens diameters and the horizontal and vertical IO angle components ($\Delta\varphi_h$ and $\Delta\varphi_v$). The position of each IO angle component is the average position of the two ommatidia per IO pair.